

# Optimal Trajectory Planning with Collision Avoidance for Autonomous Vehicle Maneuvering

Jason Zalev\*

## Abstract

To perform autonomous driving maneuvers, such as parallel or perpendicular parking, a vehicle requires continual speed and steering adjustments to follow a generated path. In consequence, the path's quality is a limiting factor of the vehicle maneuver's performance. While most path planning approaches include finding a collision-free route, optimal trajectory planning involves solving the best transition from initial to final states, minimizing the action over all paths permitted by a kinematic model. Here we propose a novel method based on sequential convex optimization, which permits flexible and efficient optimal trajectory generation. The objective is to achieve the fastest time, shortest distance, and fewest number of path segments to satisfy motion requirements, while avoiding sensor blind-spots. In our approach, vehicle kinematics are represented by a discretized Dubins model. To avoid collisions, each waypoint is constrained by linear inequalities representing closest distance of obstacles to a polygon specifying the vehicle's extent. To promote smooth and valid trajectories, the solved kinematic state and control variables are constrained and regularized by penalty terms in the model's cost function, which enforces physical restrictions including limits for steering angle, acceleration and speed. In this paper, we analyze trajectories obtained for several parking scenarios. Results demonstrate efficient and collision-free motion generated by the proposed technique.

## 1 Introduction

In autonomous parking systems, vehicle sensors capture continuous information about surrounding obstacles, including the presence of pedestrians, barriers, curbs, lane markings and other vehicles. During parking, the proximity to these obstacles is used to plan a collision-free route for entering or exiting a parking slot. Since the geometry of a slot can vary from one situation to the next, flexible planning approaches are needed to ensure optimal functionality in all circumstances.

Maneuvering approaches for automotive systems can be categorized into: direct methods [1–13], where the path and trajectory are found simultaneously; and indirect methods [14–17], where maneuvers are split into stages of path planning and path following. Indirect methods often use heuristics with efficient computation to produce a feasible path, but the resulting trajectory may be sub-optimal. This includes geometric planners, which involve creating simple paths using spline curves [14] or circular arcs and segments [15]. Direct approaches may involve higher computation to solve optimal trajectories [1–10] or use fast approximations [11]. Some approaches involve sequential convex optimization [1–8, 18–21] to handle non-linear constraints and objectives. For real-time applications, model predictive control (MPC) [12, 13] involves performing dynamic updates to path and trajectory, optimizing over a short time horizon for efficiency.

In this paper, we propose a method for optimal trajectory planning and collision avoidance in autonomous vehicles. Obstacles are represented by rectangular regions. A trajectory is defined by a series of waypoints that specify the host vehicle's kinematic state. The host

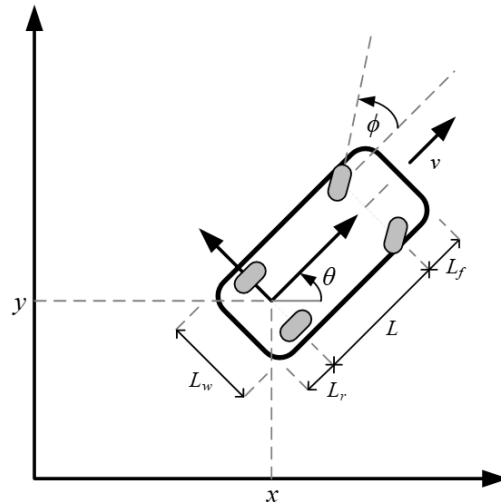


Figure 1: Vehicle geometry

\*Magna International Inc. Email: jason.zalev@magna.com

vehicle has a rectangular shape, which is extended into a convex polygon to fill gaps due to the trajectory's curvature. Constraints to avoid collision are based on finding the closest distance of the polygon to each rectangular obstacle, and penalizing waypoints that would cause any overlap. Sequential convex optimization minimizes the trajectory's total elapsed-time. The kinematic state variables are limited by upper and lower bounds, which provides flexibility to control the resulting trajectory's characteristics. Additional smoothness constraints are used to regularize the trajectory, contributing to faster convergence. As well, our approach proposes special constraints to avoid blind-spots, ensuring that low-visibility regions are swept by sensors along the trajectory, avoiding potential collisions.

## 2 Kinematic Model

We model the vehicle's trajectory using kinematic state vector  $\mathbf{x}(t)$  and control input vector  $\mathbf{u}(t)$ , according to

$$\mathbf{x}(t) = \begin{bmatrix} x(t) \\ y(t) \\ v(t) \\ a(t) \\ \theta(t) \\ \phi(t) \end{bmatrix}, \quad \mathbf{u}(t) = \begin{bmatrix} j(t) \\ \omega(t) \end{bmatrix}, \quad (2.1)$$

where  $x(t)$  and  $y(t)$  are 2D position coordinates,  $v(t)$  is velocity,  $a(t)$  is acceleration,  $\theta(t)$  is orientation,  $\phi(t)$  is steering angle,  $\omega(t)$  is steering rate and  $j(t)$  is jerk.

A state space function  $f(\mathbf{x}(t), \mathbf{u}(t), \mathbf{p})$  is constructed by specifying the time-derivative of  $\mathbf{x}(t)$ , such that

$$f(\mathbf{x}(t), \mathbf{u}(t), \mathbf{p}) = \frac{d\mathbf{x}(t)}{dt} = \begin{bmatrix} v(t) \cos \theta(t) \\ v(t) \sin \theta(t) \\ a(t) \\ j(t) \\ v(t) \tan \phi(t)/L \\ \omega(t) \end{bmatrix}, \quad (2.2)$$

which constrains the dynamics of motion and must be satisfied by any valid trajectory. Here, the vector  $\mathbf{p}$  corresponds to parameters that may be adjusted in the model. The constant  $L$  is the vehicle's wheel-base, as depicted in Figure 1.

Since equation (2.2) is non-linear, it yields a non-convex optimization problem that is difficult to solve directly. Therefore, to compute the trajectory, we use sequential convex optimization, described in Section 4, to approximate the original non-convex problem with an iterative sequence of convex sub-problems. Each sub-problem is obtained by linearizing the trajectory with respect to a reference solution, corresponding to the previous iteration's output [19–21].

To achieve this, we linearize equation (2.2) with respect to  $(\bar{\mathbf{x}}, \bar{\mathbf{u}}, \bar{\mathbf{p}})$ , which yields

$$\begin{aligned} \frac{d\mathbf{x}(t)}{dt} &= f(\mathbf{x}(t), \mathbf{u}(t), \mathbf{p}) \\ &\approx f(\bar{\mathbf{x}}(t), \bar{\mathbf{u}}(t), \bar{\mathbf{p}}) \\ &\quad + A(t)[\mathbf{x}(t) - \bar{\mathbf{x}}(t)] \\ &\quad + B(t)[\mathbf{u}(t) - \bar{\mathbf{u}}(t)] \\ &\quad + E(t)[\mathbf{p} - \bar{\mathbf{p}}] \end{aligned} \quad (2.3a)$$

$$= \begin{bmatrix} A(t) & B(t) & E(t) \end{bmatrix} \begin{bmatrix} \mathbf{x}(t) \\ \mathbf{u}(t) \\ \mathbf{p} \end{bmatrix} + \bar{\mathbf{r}}(t), \quad (2.3b)$$

where

$$\bar{\mathbf{r}}(t) = f(\bar{\mathbf{x}}, \bar{\mathbf{u}}, \bar{\mathbf{p}}) - A(t)\bar{\mathbf{x}}(t) - B(t)\bar{\mathbf{u}}(t) - E(t)\bar{\mathbf{p}}, \quad (2.3c)$$

and

$$A(t) = \nabla_{\mathbf{x}} f(\bar{\mathbf{x}}(t), \bar{\mathbf{u}}(t), \bar{\mathbf{p}}) \quad (2.4a)$$

$$B(t) = \nabla_{\mathbf{u}} f(\bar{\mathbf{x}}(t), \bar{\mathbf{u}}(t), \bar{\mathbf{p}}) \quad (2.4b)$$

$$E(t) = \nabla_{\mathbf{p}} f(\bar{\mathbf{x}}(t), \bar{\mathbf{u}}(t), \bar{\mathbf{p}}). \quad (2.4c)$$

In equation (2.3b), the reference components  $\bar{\mathbf{x}}(t)$ ,  $\bar{\mathbf{u}}(t)$  and  $\bar{\mathbf{p}}$  of (2.3a) have been collected into an overall reference vector  $\bar{\mathbf{r}}(t)$ , defined in (2.3c). As a consequence, equation (2.3b) isolates the current trajectory, which is solved in each iteration. Since  $A(t)$ ,  $B(t)$ ,  $E(t)$  and  $\bar{\mathbf{r}}(t)$  depend only on the reference components, this allows equations (2.3c) and (2.4) to be viewed as constants that are pre-computed for each iteration.

## 3 Discretization

To solve the trajectory, equation (2.1) is converted to a discretized form, represented by state variable  $\mathbf{x}_k = [x_k, y_k, v_k, a_k, \theta_k, \phi_k]^T$  with control variable  $\mathbf{u}_k = [j_k, \omega_k]^T$ , where  $k = 1 \dots N$ . Here, the discrete index  $k$  corresponds to the continuous time variable  $t = (k - 1)\Delta t$ , where  $\Delta t = t_f/N$ . This corresponds to  $N$  waypoints with uniform temporal spacing, where  $t_f$  is the time required to reach the final state. For discretization,  $t_f$  is included in the parameter set  $\mathbf{p}$ , allowing it to be solved as an unknown model variable.

For convenience, we concatenate  $\mathbf{x}_k$  and  $\mathbf{u}_k$  into the stacked vectors  $\tilde{\mathbf{x}}$  and  $\tilde{\mathbf{u}}$ , according to

$$\tilde{\mathbf{x}} = \text{vec}(\mathbf{x}_1, \mathbf{x}_2, \dots, \mathbf{x}_N), \quad (3.5a)$$

$$\tilde{\mathbf{u}} = \text{vec}(\mathbf{u}_1, \mathbf{u}_2, \dots, \mathbf{u}_N), \quad (3.5b)$$

$$\tilde{\mathbf{p}} = t_f. \quad (3.5c)$$

Using the stacked vectors from (3.5), a discretized kinematic state equation, analogous to (2.3b), can be written as

$$\underbrace{\begin{bmatrix} \tilde{A} & \tilde{B} & \tilde{E} \end{bmatrix}}_K \begin{bmatrix} \tilde{\mathbf{x}} \\ \tilde{\mathbf{u}} \\ \tilde{\mathbf{p}} \end{bmatrix} + \tilde{\mathbf{r}} = 0, \quad (3.6)$$

where  $\tilde{\mathbf{r}} = \text{vec}(\tilde{\mathbf{r}}_1, \dots, \tilde{\mathbf{r}}_N)$  is the stacked reference vector, and  $K = [\tilde{A}, \tilde{B}, \tilde{E}]$  is the overall kinematic matrix, with

$$\tilde{A} = \begin{bmatrix} A_1 & -1 & 0 & \cdots & 0 \\ 0 & \ddots & \ddots & & \vdots \\ \vdots & & \ddots & \ddots & 0 \\ 0 & \cdots & 0 & A_N & -1 \end{bmatrix} \quad (3.7a)$$

$$\tilde{B} = \begin{bmatrix} B_1^- & B_1^+ & 0 & \cdots & 0 \\ 0 & \ddots & \ddots & & \vdots \\ \vdots & & \ddots & \ddots & 0 \\ 0 & \cdots & 0 & B_N^- & B_N^+ \end{bmatrix} \quad (3.7b)$$

$$\tilde{E} = \begin{bmatrix} E_1 \\ \vdots \\ E_N \end{bmatrix}. \quad (3.7c)$$

Equation (3.7) is obtained by considering the discrete form of (2.3b), which can be written

$$\mathbf{x}_{k+1} = [A_k \quad B_k^- \quad B_k^+ \quad E_k] \begin{bmatrix} \mathbf{x}_k \\ \mathbf{u}_k \\ \mathbf{u}_{k+1} \\ \mathbf{p} \end{bmatrix} + \mathbf{r}_k. \quad (3.8)$$

Expanding for each  $k$ , and rewriting (3.8) in matrix form results in (3.7). Here,  $A_k$  describes the control-free transition from state  $\mathbf{x}_k$  to  $\mathbf{x}_{k+1}$ . A first-order hold is used to interpolate between control inputs  $\mathbf{u}_k$  and  $\mathbf{u}_{k+1}$ , involving the two control matrices  $B_k^-$  and  $B_k^+$ , similar to the approach of Malyuta et al. [21]. The matrix  $E_k$  determines the effect of  $\mathbf{p}$  on the state transition, and  $\mathbf{r}_k$  describes the reference component.

In the above equations,  $A_k$ ,  $B_k$ ,  $E_k$  and  $\mathbf{r}_k$  involve transition over the interval  $k$  to  $k+1$ . To evaluate these, we use the state transition matrix  $\Phi(t, t_0)$ , which can found by recursive numerical computation of the integral

$$\Phi(t, t_0) = I + \int_{t_0}^t A(t) \Phi(t, t_0) dt, \quad (3.9a)$$

where  $t$  is increased in small steps, starting from  $t_0$ , until  $t = t_0 + \Delta t$ , with an initial matrix  $\Phi(t_0, t_0) = I$ .

For convenience, we replace (3.9a) with  $\Phi(\tau, \tau_k)$ , changing the domain from  $t$  to  $\tau$ , where  $\tau_k = (k-1)/N$ . This captures the impact of parameter  $t_f$  on the state transition, scaling  $t$ , while keeping  $N$  fixed [20]. By direct substitution, we have

$$\Phi(\tau, \tau_k) = I + t_f \int_{\tau_k}^{\tau_{k+1}} A(t_f \tau) \Phi(\tau, \tau_k) d\tau, \quad (3.9b)$$

where  $t = t_f \tau$  and  $dt = \frac{dt}{d\tau} d\tau = t_f d\tau$ . Now, using (3.9b) to evaluate the discretization matrices (see Refs. [19–21]), we compute

$$A_k = \Phi(\tau_{k+1}, \tau_k) \quad (3.10a)$$

$$B_k^- = t_f A_k \int_{\tau_k}^{\tau_{k+1}} \Phi^{-1}(\tau, \tau_k) B(t_f \tau) \eta_-(\tau) d\tau \quad (3.10b)$$

$$B_k^+ = t_f A_k \int_{\tau_k}^{\tau_{k+1}} \Phi^{-1}(\tau, \tau_k) B(t_f \tau) \eta_+(\tau) d\tau \quad (3.10c)$$

$$E_k = t_f A_k \int_{\tau_k}^{\tau_{k+1}} \Phi^{-1}(\tau, \tau_k) E(t_f \tau) d\tau \quad (3.10d)$$

$$\mathbf{r}_k = t_f A_k \int_{\tau_k}^{\tau_{k+1}} \Phi^{-1}(\tau, \tau_k) \bar{\mathbf{r}}(t_f \tau) d\tau. \quad (3.10e)$$

Here,  $\eta_+(\tau) = \frac{\tau - \tau_k}{\Delta\tau}$  and  $\eta_-(\tau) = \frac{\tau_{k+1} - \tau}{\Delta\tau}$  are used for linear interpolation of  $B_k^-$  and  $B_k^+$ , where  $\Delta\tau = \tau_{k+1} - \tau_k$ . To solve (3.10), we evaluate (2.4), yielding

$$A(t) = \begin{bmatrix} 0 & 0 & \cos \theta & 0 & -v \sin \theta & 0 \\ 0 & 0 & \sin \theta & 0 & -v \cos \theta & 0 \\ 0 & 0 & 0 & 1 & 0 & 0 \\ 0 & 0 & 0 & 0 & 0 & 0 \\ 0 & 0 & \frac{\tan \phi}{L} & 0 & 0 & 0 \\ 0 & 0 & 0 & 0 & \frac{v}{L} \sec^2 \phi & 0 \\ 0 & 0 & 0 & 0 & 0 & 0 \end{bmatrix} \quad (3.11a)$$

$$B(t) = \begin{bmatrix} 0 & 0 \\ 0 & 0 \\ 0 & 0 \\ 1 & 0 \\ 0 & 0 \\ 0 & 1 \end{bmatrix} \quad (3.11b)$$

$$E(t) = f(\mathbf{x}(t), \mathbf{u}(t), \mathbf{p}). \quad (3.11c)$$

The matrix (3.11a) depends on states  $v(t)$ ,  $\theta(t)$  and  $\phi(t)$  of  $\mathbf{x}(t)$  according to (2.1). To compute (3.10) and (3.11), a Runge-Kutta method (see Refs. [20, 21]) is used to perform numerical integration of (3.9b) in small steps. On the interval  $\tau_k$  to  $\tau_{k+1}$ , the state vector is determined by  $\mathbf{x}(t_f \tau) = \Phi(\tau, \tau_k) \mathbf{x}_k$  and the control vector is interpolated as  $\mathbf{u}(t_f \tau) = \eta_+(\tau) \mathbf{u}_k + \eta_-(\tau) \mathbf{u}_{k+1}$ .

## 4 Trajectory Optimization

To obtain an optimal trajectory, we consider the linearized form of equation (3.6) with the unknown vector variable  $\mathbf{z} = \text{vec}(\tilde{\mathbf{x}}, \tilde{\mathbf{u}}, \tilde{\mathbf{p}})$ .

In sequential convex optimization approaches [18, 22], a non-convex optimization problem, represented as

$$\begin{aligned} & \underset{\mathbf{z}}{\text{minimize}} && g(\mathbf{z}) \\ & \text{subject to} && h(\mathbf{z}) \leq 0 \end{aligned} \quad (4.12a)$$

can be approximated with a converging sequence of convex sub-problems, given by

$$\begin{aligned} \mathbf{z}^{(i+1)} &= \mathbf{z}^{(i)} + \underset{\Delta \mathbf{z} \in \mathcal{K}_i}{\text{argmin}} \nabla g(\mathbf{z}^{(i)})^T \Delta \mathbf{z} \\ & \text{subject to} \nabla h(\mathbf{z}^{(i)})^T \Delta \mathbf{z} \leq -h(\mathbf{z}^{(i)}), \end{aligned} \quad (4.12b)$$

where  $\mathbf{z}^{(i+1)}$  is the solution of iteration  $i + 1$ . Here, the non-linear objective  $g(\mathbf{z})$  and constraint  $h(\mathbf{z})$  of (4.12a) are linearized in (4.12b) by computing gradients  $\nabla g(\mathbf{z})$  and  $\nabla h(\mathbf{z})$  with respect to previous solution  $\mathbf{z}^{(i)}$  (starting with initial solution  $\mathbf{z}^{(0)}$ ).

In (4.12b), the unknown variable  $\Delta \mathbf{z}$ , which is solved, corresponds to the change in solution  $\mathbf{z}^{(i+1)} - \mathbf{z}^{(i)}$ , updating the result in each iteration. This sequence of solutions will converge to a local minimum when  $\Delta \mathbf{z}$  is confined to a suitable trust region  $\mathcal{K}_i$  anchored at  $\mathbf{z}^{(i)}$  [22]. A penalized trust region for  $\mathcal{K}_i$  can be implemented using an  $\alpha$ -weighted norm  $\|\Delta \mathbf{z}\|_\alpha$ , where  $\alpha$  specifies a weighting between elements of  $\Delta \mathbf{z}$ . The weighting is selected to normalize each element to its range of valid parameters, scaling the step-sizes along individual dimensions for improved convergence.

To solve an optimal trajectory, we use equation (4.12) with the  $i$ -th iteration specified by

$$\begin{bmatrix} \tilde{\mathbf{x}}^{(i+1)} \\ \tilde{\mathbf{u}}^{(i+1)} \\ t_f^{(i+1)} \end{bmatrix} = \underset{\tilde{\mathbf{x}}, \tilde{\mathbf{u}}, t_f}{\text{argmin}} t_f + \varphi(\tilde{\mathbf{x}}, \tilde{\mathbf{u}}) + \left\| \begin{bmatrix} \tilde{\mathbf{x}} - \tilde{\mathbf{x}}^{(i)} \\ \tilde{\mathbf{u}} - \tilde{\mathbf{u}}^{(i)} \\ t_f - t_f^{(i)} \end{bmatrix} \right\|_\alpha^2 \quad (4.13a)$$

$$\text{subject to} \quad K \begin{bmatrix} \tilde{\mathbf{x}} \\ \tilde{\mathbf{u}} \\ t_f \end{bmatrix} + \tilde{\mathbf{r}} = 0 \quad (4.13b)$$

$$M\tilde{\mathbf{x}} + \mathbf{b} \leq 0 \quad (4.13c)$$

$$\mathbf{x}_1 = \mathbf{x}_{\text{init}}, \quad \mathbf{u}_N = \mathbf{u}_{\text{final}} \quad (4.13d)$$

$$\mathbf{u}_1 = \mathbf{u}_{\text{init}}, \quad \mathbf{x}_N = \mathbf{x}_{\text{final}} \quad (4.13e)$$

$$\begin{bmatrix} \mathbf{x}_{\min} \\ \mathbf{u}_{\min} \end{bmatrix} \leq \begin{bmatrix} \mathbf{x}_k \\ \mathbf{u}_k \end{bmatrix} \leq \begin{bmatrix} \mathbf{x}_{\max} \\ \mathbf{u}_{\max} \end{bmatrix} \quad (4.13f)$$

$$t_f^{\min} \leq t_f \leq t_f^{\max} \quad (4.13f)$$

The first term of (4.13a) minimizes the time to reach

final state  $t_f$ . The second term  $\varphi(\tilde{\mathbf{x}}, \tilde{\mathbf{u}})$  is used to regularize the state and control variables. This promotes smoothness and minimizes energy used in the trajectory, and also results in faster convergence. The third term  $\|\cdot\|_\alpha$  penalizes results far from the previous solution, with each variable weighted by vector  $\alpha$ . Equation (4.13b) is an equality constraint to ensure valid dynamics corresponding to equation (3.6). Collision avoidance is implemented with (4.13c), as described in Section 5. Equation (4.13d) is used to fix the position of the initial and final waypoints and control variables. Equation (4.13e) ensures that each state and control variable is bounded between minimum and maximum values for  $k = 1 \dots N$ . Equation (4.13f) sets limits on  $t_f$ .

## 5 Collision Avoidance

In this section, we formulate the collision avoidance constraints of equation (4.13c). This involves specifying one constraint for each waypoint with respect to each obstacle. In each iteration of equation (4.13), it is efficient to compute  $d_{kj}$ , the closest distance from the  $j$ -th obstacle to the polygonal boundary surrounding waypoint  $x_k$ .

If  $d_{kj}$  is positive, this indicates a safe distance to the vehicle, whereas a negative value indicates penetration into the obstacle. An individual constraint is given by

$$d_{kj} + \nabla d_{kj}^T \mathbf{x}_k \geq 0, \quad (5.14)$$

where the gradient  $\nabla d_{kj}$ , taken with respect  $\mathbf{x}_k$ , represents how variations in the state variables impact distance to the object, as described below.

For collision avoidance, using a polygonal boundary permits filling of gaps that result from sampling and curvature of successive waypoints, which is apparent in Figures 2 and 4, where spacing between adjacent rectangles creates a “sawtooth” pattern. To fill in these gaps, polygon  $k$  is taken as the convex hull of two rectangles at adjacent waypoints  $\mathbf{x}_k$  and  $\mathbf{x}_{k+1}$ , transformed according to the vehicle’s position and orientation. As depicted in Figure 1, the vehicle has length  $L + L_f + L_r$  and width  $L_w$ , where  $L_f$  and  $L_r$  are the front and rear overhang and  $L$  is the wheel base.

The vehicle polygon consists of a list of edges and vertices that surround waypoint  $k$ . The  $j$ -th obstacle is represented by a rectangle, with center position  $(x_j, y_j)$ , length  $a_j$ , width  $b_j$  and orientation  $\psi_j$ . To compute the closest point in an efficient way, the polygon is rotated into the  $j$ -th obstacle’s principal coordinate frame, according to

$$\begin{bmatrix} g_x \\ g_y \end{bmatrix} = R^{-1}(\psi_j) \begin{bmatrix} p_x - x_j \\ p_y - y_j \end{bmatrix}, \quad (5.15)$$

where  $(p_x, p_y)$  is a polygon vertex. The rotation matrix is

$$R(\psi_j) = \begin{bmatrix} \cos(\psi_j) & -\sin(\psi_j) \\ \sin(\psi_j) & \cos(\psi_j) \end{bmatrix}. \quad (5.16)$$

When the polygon does not intersect the rectangle, the closest point  $(\tilde{g}_x, \tilde{g}_y)$  is found by identifying the minimum distance between the polygon's edges and the rectangle's sides using separating-axis projections. However, if any vertices are found within the rectangle (i.e.,  $|g_x| < a_j$  and  $|g_y| < b_j$ ), then  $(\tilde{g}_x, \tilde{g}_y)$  is set to their average position. Otherwise, if an edge has two intersections with the rectangle, their midpoint is used.

Equation (5.14) is specified, using the closest point, according to

$$d_{kj} = \begin{cases} \sqrt{(d_{kj}^x)^2 + (d_{kj}^y)^2}, & |\tilde{g}_x| > a_0 \text{ or } |\tilde{g}_y| > b_0, \\ \mathbf{n}^T \begin{bmatrix} \tilde{g}_x - a_j s_x \\ \tilde{g}_y - b_j s_y \end{bmatrix}, & \text{otherwise} \end{cases} \quad (5.17a)$$

where  $d_{kj}^x = \max(0, \tilde{g}_x - a_j, -\tilde{g}_x - a_j)$  and  $d_{kj}^y = \max(0, \tilde{g}_y - b_j, -\tilde{g}_y - b_j)$ . Here, for brevity, we set  $s_x = \text{sign}(\tilde{g}_x)$  and  $s_y = \text{sign}(\tilde{g}_y)$ . The gradient is computed as

$$\nabla d_{kj} = [\tilde{n}_1, \tilde{n}_2, 0, 0, \tilde{n}_2 \cos(\theta_k) - \tilde{n}_1 \sin(\theta_k), 0]^T, \quad (5.17b)$$

where  $\theta_k$  is the vehicle orientation at waypoint  $\mathbf{x}_k$ . The direction vector  $\tilde{\mathbf{n}} = (\tilde{n}_1, \tilde{n}_2)$  is

$$\tilde{\mathbf{n}} = R(\psi_j) \mathbf{n}, \quad (5.18)$$

where

$$\mathbf{n} = \begin{cases} \frac{(\tilde{g}_x, \tilde{g}_y)}{\|(\tilde{g}_x, \tilde{g}_y)\|}, & |\tilde{g}_x| > a_j \text{ or } |\tilde{g}_y| > b_j, \\ \frac{(s_x, s_y)}{\|(s_x, s_y)\|}, & \max(||\tilde{g}_x| - a_j|, ||\tilde{g}_y| - b_j|) \leq \epsilon \\ (s_x, 0), & \left| \frac{\tilde{g}_x}{a_j} \right| \leq \left| \frac{\tilde{g}_y}{b_j} \right| \\ (0, s_y), & \text{otherwise.} \end{cases} \quad (5.19)$$

In equation (5.19), when there is no collision,  $\mathbf{n}$  represents the direction of the closest point to the obstacle. If a collision will occur, constraint (5.14) becomes active, pushing the waypoint in direction  $\mathbf{n}$  for the next iteration. To achieve effective performance, if  $(\tilde{g}_x, \tilde{g}_y)$  is inside the obstacle, when it falls within distance  $\epsilon$  of a corner,  $\mathbf{n}$  is oriented at a  $45^\circ$  angle; otherwise,  $\mathbf{n}$  will be oriented to push away the waypoint in a direction perpendicular to the rectangle's closest side. In this manner, by snapping to angles in increments of  $45^\circ$

relative to  $\psi_j$ , the gradient  $\nabla d_{kj}$  remains more stable between successive iterations, which reduces oscillation, leading to faster convergence.

The collision avoidance constraints of equation (4.13c) are obtained as

$$\begin{aligned} M &= \text{diag}(M_1, \dots, M_N), \\ \mathbf{b} &= \text{vec}(\mathbf{b}_1, \dots, \mathbf{b}_N), \end{aligned} \quad (5.20a)$$

where each sub-matrix  $M_k$  and column vector  $\mathbf{b}_k$ , for  $k = 1 \dots N$ , is defined as

$$\begin{aligned} M_k &= [\nabla d_{k1}, \dots, \nabla d_{kJ}]^T, \\ \mathbf{b}_k &= [d_{k1}, \dots, d_{kJ}]^T. \end{aligned} \quad (5.20b)$$

Thus, row  $j$  in (5.20b) corresponds to equation (5.17) for the  $j$ -th obstacle and  $k$ -th waypoint.

## 6 Blind Spot Avoidance

In general, it is undesirable for an autonomous vehicle to move into an area that has been left unchecked by sensors without confirming that no obstacle is present. While sensor placement provides sufficient coverage to detect obstacles in most scenarios, potential issues can arise due to sensor latency, sensor blockage and high steering angle. In some situations, there is potential for sides of the host vehicle to enter blind-spots when it is turning. As well, when the host vehicle or obstacle are moving, sensors may have insufficient time to distinguish a sudden detection from background noise, despite proper coverage. Moreover, sensor near-field zones may have limitations in detecting obstacles or estimating their distances.

In this section we propose constraints so the generated trajectory will avoid passing through blind spots. The approach involves using a known spatial map of the sensor field-of-view, which is used to maintain a map of regions that remain unchecked at each waypoint in the trajectory. In each iteration of equation 4.13, modified bounds constraints are computed to prevent the vehicle from traversing through the unchecked region.

In our approach, the sensor field-of-view is modeled as an image mask, which is given by

$$V(\mathbf{q}) = \begin{cases} 0, & \text{if } \mathbf{q} \text{ is a blind spot,} \\ 1, & \text{if } \mathbf{q} \text{ is visible,} \end{cases} \quad (6.21)$$

where  $\mathbf{q} = (q_x, q_y)$  is a coordinate in the host vehicle's local frame. The unchecked region for waypoint  $k$  is

$$U_k(\mathbf{r}) = 1 - C_k(\mathbf{r}), \quad (6.22a)$$

where the checked region  $C_k(\mathbf{r})$  is formed by transforming  $V(\mathbf{q})$  relative to waypoint  $k$ , and computing a union

with the previous checked region  $C_{k-1}(\mathbf{r})$ . Thus,

$$C_k(\mathbf{r}) = C_{k-1}(\mathbf{r}) \cup V(R_{\theta_k}(\mathbf{r} - \mathbf{r}_k)). \quad (6.22b)$$

Here,  $\mathbf{r} = (r_x, r_y)$  is a coordinate in the global frame,  $\mathbf{r}_k = (x_k, y_k)$  is the vehicle's position and  $R_{\theta_k} = R(\theta_k)$  is a rotation by vehicle orientation  $\theta_k$ . The initial  $C_0$  is set to 1 in a region surrounding the host vehicle, and 0 elsewhere.

To compute modified bounds constraints, specific increases or decreases to  $x_k$ ,  $y_k$  or  $\theta_k$  are found that would cause the host vehicle's boundary polygon to intersect  $U_k(\mathbf{r})$ . In particular, constraint (4.13e) is modified so  $\mathbf{x}_k^{\min}$  and  $\mathbf{x}_k^{\max}$  depend on  $k$ . The new limits are given by

$$\begin{aligned} x_k^{\min} &= \max(x_k^{\min}, x_k - \Delta x_k^-) \\ y_k^{\min} &= \max(y_k^{\min}, y_k - \Delta y_k^-) \\ \theta_k^{\min} &= \max(\theta_k^{\min}, \theta_k - \Delta \theta_k^-) \end{aligned} \quad (6.23a)$$

and

$$\begin{aligned} x_k^{\max} &= \min(x_k^{\max}, x_k + \Delta x_k^+) \\ y_k^{\max} &= \min(y_k^{\max}, y_k + \Delta y_k^+) \\ \theta_k^{\max} &= \min(\theta_k^{\max}, \theta_k + \Delta \theta_k^+) \end{aligned} \quad (6.23b)$$

where  $\Delta x_k^\pm$ ,  $\Delta y_k^\pm$  and  $\Delta \theta_k^\pm$  are the smallest displacements for the vehicle polygon to reach a non-zero in  $U_k(\mathbf{r})$ .

## 7 Results and Discussion

In this section, results are presented for our optimal trajectory planning method in various parking scenarios. To achieve this, a custom implementation of equation (4.13) was written using CVXPYGEN [23], a Python-based solver-generator that produces efficient C++ output for minimizing optimization problems. The discretization of equation (3.10) was performed using the SCVX Toolbox [20] in Matlab, which was used to call the compiled solver. A custom graphical user interface (GUI) was created to specify vehicle and obstacle geometry, along with the kinematic constraints of equations (4.13d) to (4.13f).

Results are demonstrated in Figures 2 to 4, which illustrate the vehicle's path and the corresponding state and control variables over time. In each figure, the vehicle's path is depicted with a marker representing each waypoint, and a corresponding rectangle to indicate the vehicle's position and orientation at each step. Boundaries that define the obstacles are also shown. The plotted variables include:  $x(t)$ , the x-coordinate of the vehicle's position;  $y(t)$ , the y-coordinate of the vehicle's position;  $v(t)$ , the vehicle's velocity;  $a(t)$ , the vehicle's

acceleration;  $\theta(t)$ , the vehicle's orientation angle;  $\phi(t)$ , the steering angle;  $j(t)$ , the jerk (rate of change of acceleration); and  $\omega(t)$ , the steering rate.

Figure 2 shows the trajectory generated for a rear-in perpendicular parking maneuver. Here, the "L"-shaped driving region is formed by four rectangular obstacles.

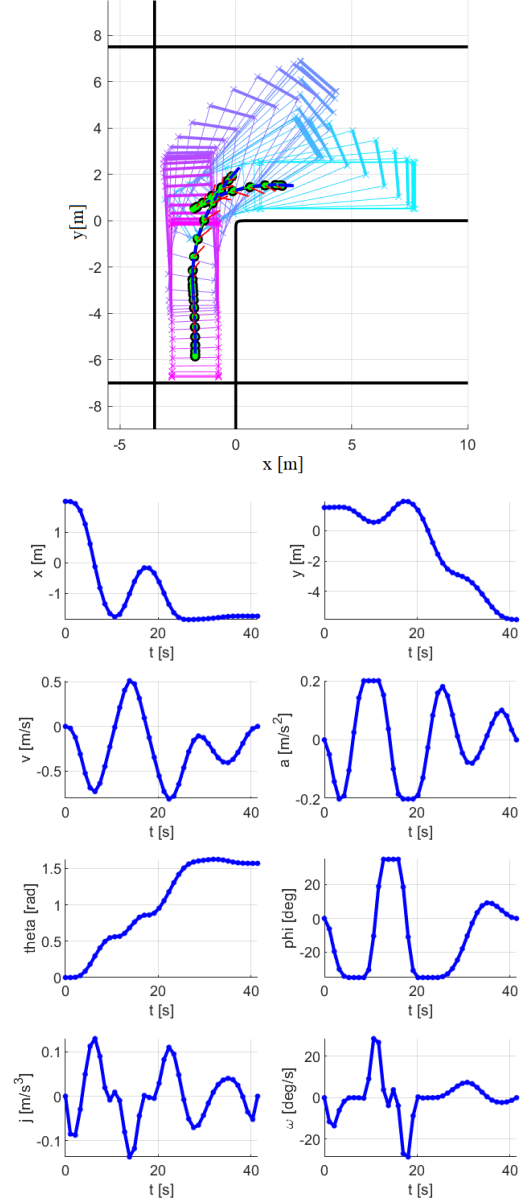


Figure 2: Rear-in perpendicular parking maneuver. The plots show state and control variables over time, demonstrating adjustments for a smooth and collision-free trajectory into a perpendicular slot. The vehicle boundary transitions from cyan (initial position) to magenta (final position).

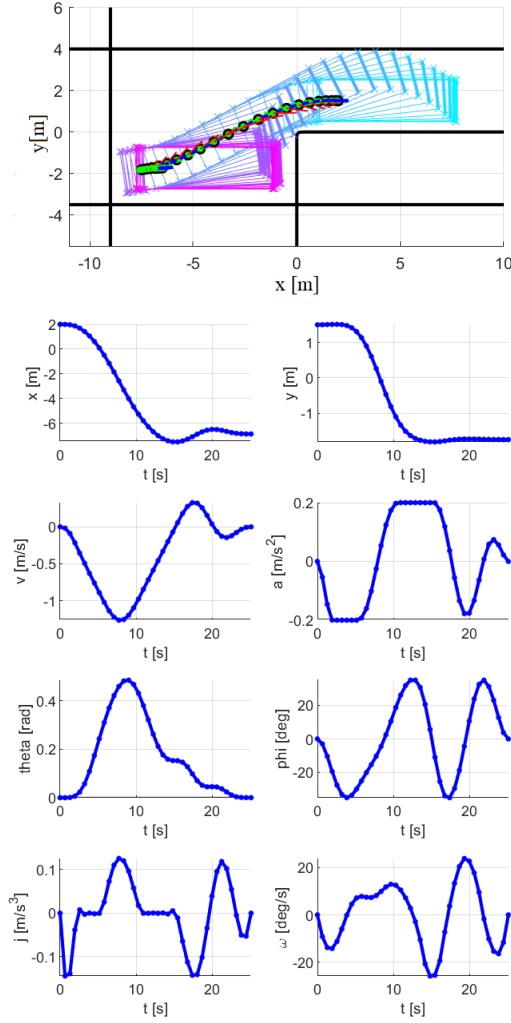


Figure 3: Rear-in parallel parking maneuver. The plots illustrate adjustments in position, velocity, and steering to align parallel to the curb and fit into the parking slot. The vehicle boundary transitions from cyan (initial position) to magenta (final position).

Plots of the state and control variable demonstrate how the vehicle adjusts its speed and steering to achieve a smooth and collision-free trajectory into the parking slot. A rear-in parallel parking maneuver is shown in Figure 3. In Figure 4, the results for a parallel park-in maneuver are shown. Here, the vehicle must avoid going off the road when moving forward, then it backs into a slot between two cars.

These results demonstrate the effectiveness of our proposed method for generating optimal and collision-free trajectories. Successful navigation into and out of parking slots was achieved while adhering to the constraints on state and control variables.

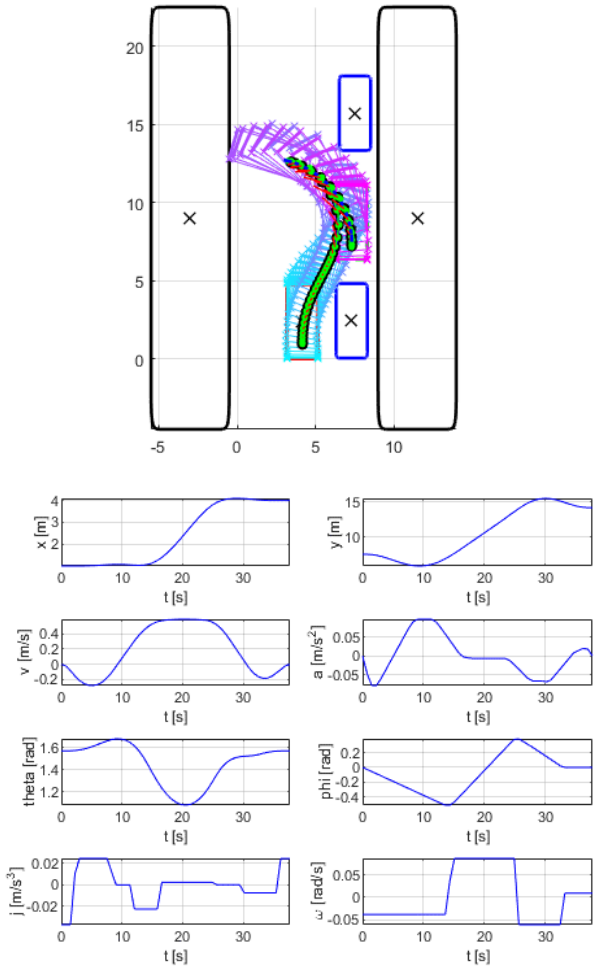


Figure 4: Parallel park-in maneuver. The host vehicle avoids going off road when moving forward, before backing into a slot between two cars. The vehicle boundary transitions from cyan (initial position) to magenta (final position).

## 8 Conclusion

This paper presented a novel method for optimal trajectory planning. Using sequential convex optimization, we generated efficient and collision-free trajectories for various parking scenarios. The proposed approach handles vehicle kinematics, obstacle avoidance, and sensor blind-spots, ensuring smooth and feasible paths. The results demonstrated the method's capability to navigate complex parking maneuvers, validating its practical applicability and efficiency. Future work may explore real-time implementation and integration with advanced sensor technologies to further enhance the system's robustness and performance.

## References

- [1] B. Li, K. Wang, and Z. Shao, "Time-optimal maneuver planning in automatic parallel parking using a simultaneous dynamic optimization approach," *IEEE Transactions on Intelligent Transportation Systems*, vol. 17, no. 11, pp. 3263–3274, 2016.
- [2] D. Qiu, D. Qiu, B. Wu, M. Gu, and M. Zhu, "Hierarchical control of trajectory planning and trajectory tracking for autonomous parallel parking," *IEEE Access*, vol. 9, pp. 94 845–94 861, 2021.
- [3] R. Chai, A. Tsourdos, A. Savvaris, S. Chai, and Y. Xia, "Two-stage trajectory optimization for autonomous ground vehicles parking maneuver," *IEEE Transactions on Industrial Informatics*, vol. 15, no. 7, pp. 3899–3909, 2018.
- [4] B. Li, T. Acarman, Y. Zhang, Y. Ouyang, C. Yaman, Q. Kong, X. Zhong, and X. Peng, "Optimization-based trajectory planning for autonomous parking with irregularly placed obstacles: A lightweight iterative framework," *IEEE Transactions on Intelligent Transportation Systems*, vol. 23, no. 8, pp. 11 970–11 981, 2021.
- [5] B. Li, T. Acarman, Y. Zhang, L. Zhang, C. Yaman, and Q. Kong, "Tractor-trailer vehicle trajectory planning in narrow environments with a progressively constrained optimal control approach," *IEEE Transactions on Intelligent Vehicles*, vol. 5, no. 3, pp. 414–425, 2019.
- [6] C. Sun, Q. Li, B. Li, and L. Li, "A successive linearization in feasible set algorithm for vehicle motion planning in unstructured and low-speed scenarios," *IEEE Transactions on Intelligent Transportation Systems*, vol. 23, no. 4, pp. 3724–3736, 2021.
- [7] Z. Zhu, E. Schmerling, and M. Pavone, "A convex optimization approach to smooth trajectories for motion planning with car-like robots," in *2015 54th IEEE conference on decision and control (CDC)*. IEEE, 2015, pp. 835–842.
- [8] A. Boyali, S. Thompson, and D. Wong, "Applications of successive convexification in autonomous vehicle planning and control," in *2020 4th International Conference on Automation, Control and Robots (ICACR)*. IEEE, 2020, pp. 88–95.
- [9] I. Noreen, A. Khan, and Z. Habib, "Optimal path planning using rrt\* based approaches: a survey and future directions," *International Journal of Advanced Computer Science and Applications*, vol. 7, no. 11, 2016.
- [10] S. Karaman and E. Frazzoli, "Optimal kinodynamic motion planning using incremental sampling-based methods," in *49th IEEE conference on decision and control (CDC)*. IEEE, 2010, pp. 7681–7687.
- [11] P. Zips, M. Bock, and A. Kugi, "A fast motion planning algorithm for car parking based on static optimization," in *2013 IEEE/RSJ International Conference on Intelligent Robots and Systems*. IEEE, 2013, pp. 2392–2397.
- [12] R. Verschuere, S. De Bruyne, M. Zanon, J. V. Frasch, and M. Diehl, "Towards time-optimal race car driving using nonlinear mpc in real-time," in *53rd IEEE conference on decision and control*. IEEE, 2014, pp. 2505–2510.
- [13] C. Liu, S. Lee, S. Varnhagen, and H. E. Tseng, "Path planning for autonomous vehicles using model predictive control," in *2017 IEEE Intelligent Vehicles Symposium (IV)*. IEEE, 2017, pp. 174–179.
- [14] F. Gómez-Bravo, F. Cuesta, A. Ollero, and A. Viguria, "Continuous curvature path generation based on  $\beta$ -spline curves for parking manoeuvres," *Robotics and autonomous systems*, vol. 56, no. 4, pp. 360–372, 2008.
- [15] J. Reeds and L. Shepp, "Optimal paths for a car that goes both forwards and backwards," *Pacific journal of mathematics*, vol. 145, no. 2, pp. 367–393, 1990.
- [16] T. Lipp and S. Boyd, "Minimum-time speed optimisation over a fixed path," *International Journal of Control*, vol. 87, no. 6, pp. 1297–1311, 2014.
- [17] X. Zhang, A. Liniger, and F. Borrelli, "Optimization-based collision avoidance," *IEEE Transactions on Control Systems Technology*, vol. 29, no. 3, pp. 972–983, 2020.
- [18] D. Malyuta, T. P. Reynolds, M. Szmuk, T. Lew, R. Bonalli, M. Pavone, and B. Açikmeşe, "Convex optimization for trajectory generation: A tutorial on generating dynamically feasible trajectories reliably and efficiently," *IEEE Control Systems Magazine*, vol. 42, no. 5, pp. 40–113, 2022.
- [19] Y. Mao, M. Szmuk, X. Xu, and B. Açikmeşe, "Successive convexification: A superlinearly convergent algorithm for non-convex optimal control problems," *arXiv preprint arXiv:1804.06539*, 2018.
- [20] T. Reynolds, D. Malyuta, M. Mesbahi, B. Açikmeşe, and J. M. Carson, "A real-time algorithm for non-convex powered descent guidance," in *AIAA Scitech 2020 Forum*, 2020, p. 0844.
- [21] D. Malyuta, T. P. Reynolds, M. Szmuk, M. Mesbahi, B. Açikmeşe, and J. M. Carson III, "Discretization performance and accuracy analysis for the powered descent guidance problem," in *AIAA Scitech 2019 Forum*, 2019, pp. 1–20.
- [22] Y.-x. Yuan, "Recent advances in trust region algorithms," *Mathematical Programming*, vol. 151, pp. 249–281, 2015.
- [23] M. Schaller, G. Banjac, S. Diamond, A. Agrawal, B. Stellato, and S. Boyd, "Embedded code generation with cvxpy," *IEEE Control Systems Letters*, vol. 6, pp. 2653–2658, 2022.